UNIVERSITY OF
Southampton
School of Engineering Sciences

Aerodynamics & Flight Mechanics Research Group

Direct Numerical Simulation of a Sonic Round Jet in a Turbulent Supersonic Cross Flow

J. Castagna and N.D. Sandham

Technical Report AFM- 10/01

January 2010

UNIVERSITY OF SOUTHAMPTON

SCHOOL OF ENGINEERING SCIENCES

AERODYNAMICS AND FLIGHT MECHANICS RESEARCH GROUP

Direct Numerical Simulation of a Sonic Round Jet in a Turbulent Supersonic Cross Flow

by

J. Castagna and N.D. Sandham

AFM Report No. AFM 10/01 (c)

January 2010

Direct Numerical Simulation of a Sonic Round Jet in a Turbulent Supersonic Cross Flow

Jony Castagna and Neil D. Sandham
University of Southampton

Internal Report

January 30, 2010

Abstract

A direct numerical simulation of a round under-expanded sonic jet in turbulent supersonic cross flow has been carried out. The objective is to investigate the mixing mechanism which occurs downstream the jet by use of a passive scalar variable. The Navier-Stokes equations in the cylindrical geometry are solved by use of multiblock overlapping meshes. The method has been validated with a laminar flow in pipe and a convergence study has been carried out. The inlet profile of the cross flow is generated with a precursor turbulent channel at same Reynolds number ($Re_\tau = 180$) and Mach number ($M_{cl} = 1.6$). In order to reproduce physical conditions more similar to a supersonic combustion ramjet (SCRAM-JET) chamber, a heat sink $\dot{Q}$ has been added in the energy equation. The effect is to decrease the bulk temperature to a lower value than the wall temperature. A test case at injection angle $\theta = 90^\circ$ and jet to cross flow momentum flux ratio $J = 1$ has been carried out. Data have been compared with the results obtained from a similar configuration where the jet inlet is obtained without the nozzle geometry. Some difference are observed in the penetration height of the passive scalar, but the flow topology is quite similar for both cases. A parametric study at different angle θ and jet to cross flow momentum ration J is planned as future work.

Keywords: DNS, multiblock structured mesh, turbulent plane channel, passive scalar

Contents

1 Introduction.

Jets in cross flow are very common in practical applications such as air-breathing engines, film cooling of blades, dispersion of pollutants in the atmosphere, etc. In supersonic combustion ramjet (SCRAMJET) applications, where the cross flow is supersonic, the understanding of the mixing mechanism plays an important role in the design of the combustor chamber.

Typically, when an under-expanded sonic jet is injected into a supersonic cross flow, 3D-shocks appear and boundary layer separation occurs (see Figure 1[1, 2]). The jet expands through a Prandtl-Meyer fan at the jet orifice and then is compressed by the barrel shock (Mach disk). The bow shock ahead the jet is due to the blockage of the flow and it causes upstream boundary layer separation. The separated flow leads to the formation of a horseshoe vortex, while downstream of the jet a counter-rotating vortex pair is formed.

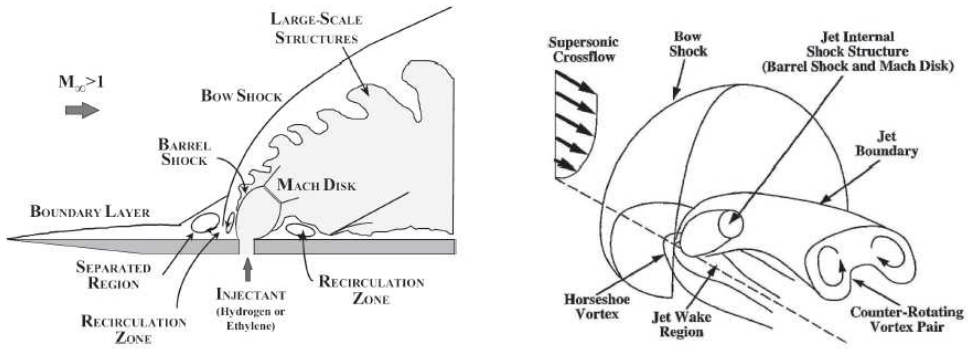

Figure 1: Schematics of an under-expanded jet in a supersonic cross flow.[1, 2]

Temporally resolved flow visualizations of jet in supersonic cross flow (hereafter JISCF) using non-reactive[2, 5] and combustible jet gases[1] have been provided in the past. Moreover, detailed measurement of the velocity flow field[3] and of the time-averaged wall pressure[4] have been carried out. Recent work using an ethylene jet in a supersonic air cross flow at Mach 2 have been carried out[7]. The experiments have been conducted at different jet injection angles, different jet diameters and different jet to cross flow momentum flux ratios. Moreover, after comparison with numerical simulations the authors suggested a correlation between the penetration high, the jet angle, the momentum flux ratio and the jet diameter. However, due to the high speed involved and the complex mechanism described above, experimental investigations on JISCF are generally difficult to carry out and only data for certain 2D plane have been obtained.

The numerical simulation seems to be a useful approach to understanding this complex phenomenon. Reynolds Averaged Navier-Stokes (RANS) simulations of JISCF based on a second-order Reynolds Stress Turbulent Model (RSTM) and a $K-\epsilon$ model have been carried out[8] . The main flow features are correctly captured and the superiority of the RSTM relative to the $K-\epsilon$ model in predicting physically correct behavior of the turbulent cross flow shear stress has been proven. However, no information on the structures of the flow was obtained due to time averaging characteristic of the RANS approach. Information on the large-scale structures has been provided by large-eddy simulation (LES) and detached-eddy simulation (DES)[9, 10] . However, due to the low-order upwinding finite

volume schemes adopted (Roe's flux difference splitting and Steger-Warming flux vector splitting for the shock capturing), the turbulent eddy structures were not correctly solved as those schemes are too dissipative for an LES approach. Better results have been recently obtained using high-order compact differencing/filtering schemes coupled with a localized artificial diffusivity method in the context of LES[6]. The bow shock and the barrel shock are qualitatively correctly reproduced and important information on the windward and leeward side of the jet are provided. Statistics are also in agreement with the experimental results [3] . However, the cross flow is laminar and a grid refinement study with turbulent inflow conditions is necessary to improve the results obtained.

In the present work, we carried out direct numerical simulations of JISCF. The goal is to provide information on the turbulent mixing mechanism which may then be useful for the improvement of turbulent models in LES and RANS techniques. The round jet has been simulated using a multiblock overlapping grid, validated with laminar simulations of flow in a pipe. The cross flow is turbulent at $Re_\tau = 180$ and $M_{cl} = 1.6$ and the inlet is provided by a precursor turbulent channel. A sink of energy has been used in the precursor simulation in order to reproduce flow conditions more closer SCRAMJET applications (i.e. hot walls and cooles bulk region). Different injection angles and flux momentum ratios have been simulated. The results are compared with a configuration where the nozzle part is substituted by a fixed profile at the wall of the cross flow.

The report is divided as follows: firstly we give a description of the mathematical models and numerical features used in the present work. The multiblock overlapping mesh is then described and results on the laminar flow in a pipe are presented. The next section is dedicated to the inflow and boundary conditions for the jet and the cross flow. Results on the precursor turbulent channel with the sink of energy are presented. Then, comparisons between the JISCF obtained with and without the nozzle are shown for the case at injection angle of 90 degree and flux momentum ratio of one. Finally, a parametric study at different injection angles and flux momentum ratio is presented and conclusions are given in a final summary section.

2 Mathematical models.

2.1 Governing equations.

In non-dimensional form, the conservation equations for a compressible fluid are:

$$\frac{\partial \rho}{\partial t} + \frac{(\partial \rho u_i)}{\partial x_i} = 0, \tag{1}$$

$$\frac{\partial (\rho u_i)}{\partial t} + \frac{\partial (\rho u_i u_j)}{\partial x_j} = -\frac{\partial p}{\partial x_i} - \frac{1}{Re}\frac{\partial \tau_{ij}}{\partial x_j}, \tag{2}$$

$$\frac{\partial E_{tot}}{\partial t} + \frac{\partial [(E_{tot}+p)u_j]}{\partial x_j} = -\frac{1}{(\gamma-1)RePrM^2}\frac{\partial}{\partial x_j}\left(\mu \frac{\partial T}{\partial x_j}\right) + \frac{1}{Re}\frac{\partial u_j \tau_{ij}}{\partial x_i}, \tag{3}$$

$$\frac{\partial (\rho C)}{\partial t} + \frac{\partial (\rho C u_j)}{\partial x_j} = \frac{1}{Sc}\frac{\partial^2 C}{\partial x_j^2}, \tag{4}$$

where $i, j = 1, 2, 3$ are the coordinate indices, u_i the velocity components, p the static

pressure, C the concentration of the passive scalar, T the temperature and τ_{ij} the stress tensor components. Re, Pr, Sc and M are the Reynolds, Prandtl, Schmidt and Mach number, respectively, E_{tot} is the total energy, γ the specific heat ratio and μ the fluid viscosity. The fluid is assumed to be and ideal gas and Newtonian. This defines the correlation between stress tensor and velocity field. We take $\gamma = 1$ and $Pr = 0.72$.

When a coordinate transformation technique is applied, the above equations are normally re-written in the following hyperbolic vector form:

$$\frac{\partial U_1}{\partial t} + \frac{\partial F_1}{\partial \xi} + \frac{\partial G_1}{\partial \eta} + \frac{\partial H_1}{\partial \zeta} = 0, \tag{5}$$

where:

$$U_1 = JU \tag{6}$$

$$F_1 = \left(JF\frac{\partial \xi}{\partial x} + JG\frac{\partial \xi}{\partial y} + JH\frac{\partial \xi}{\partial z} \right) \tag{7}$$

$$G_1 = \left(JF\frac{\partial \eta}{\partial x} + JG\frac{\partial \eta}{\partial y} + JH\frac{\partial \eta}{\partial z} \right) \tag{8}$$

$$H_1 = \left(JF\frac{\partial \zeta}{\partial x} + JG\frac{\partial \zeta}{\partial y} + JH\frac{\partial \zeta}{\partial z} \right), \tag{9}$$

and

$$U = \begin{pmatrix} \rho \\ \rho u \\ \rho v \\ \rho w \\ E_{tot} \end{pmatrix}, \tag{10}$$

$$F = \begin{pmatrix} \rho u \\ \rho uu + p - \tau_{xx} \\ \rho uv - \tau_{xy} \\ \rho uw - \tau_{xz} \\ (E_{tot} + p)u + q_x - \tau_{xx}u - \tau_{xy}v - \tau_{xz}w \end{pmatrix}, \tag{11}$$

$$G = \begin{pmatrix} \rho v \\ \rho vu - \tau_{yx} \\ \rho vv + p - \tau_{yy} \\ \rho vw - \tau_{yz} \\ (E_{tot} + p)v + q_y - \tau_{yx}u - \tau_{yy}v - \tau_{yz}w \end{pmatrix}, \tag{12}$$

$$H = \begin{pmatrix} \rho w \\ \rho wu - \tau_{zx} \\ \rho wv - \tau_{zy} \\ \rho ww + p - \tau_{zz} \\ (E_{tot} + p)w + q_z - \tau_{zx}u - \tau_{zy}v - \tau_{zz}w \end{pmatrix}. \tag{13}$$

However, if 3D-curvilinear transformations are involved, the above form can introduce some errors when a central finite difference scheme is applied[23]. The source of the numerical error is in the non-cancelation of the following terms:

$$I_1 = \frac{\partial}{\partial \xi}\left(J\frac{\partial \xi}{\partial x}\right) + \frac{\partial}{\partial \eta}\left(J\frac{\partial \eta}{\partial x}\right) + \frac{\partial}{\partial \zeta}\left(J\frac{\partial \zeta}{\partial x}\right) = 0, \tag{14}$$

$$I_2 = \frac{\partial}{\partial \xi}\left(J\frac{\partial \xi}{\partial y}\right) + \frac{\partial}{\partial \eta}\left(J\frac{\partial \eta}{\partial y}\right) + \frac{\partial}{\partial \zeta}\left(J\frac{\partial \zeta}{\partial y}\right) = 0, \tag{15}$$

$$I_3 = \frac{\partial}{\partial \xi}\left(J\frac{\partial \xi}{\partial z}\right) + \frac{\partial}{\partial \eta}\left(J\frac{\partial \eta}{\partial z}\right) + \frac{\partial}{\partial \zeta}\left(J\frac{\partial \zeta}{\partial z}\right) = 0. \tag{16}$$

Different methods have been proposed in order to guarantee the validity of eqns. (14)-(16) [23, 20]. However, we note that eqn. (5) can be is obtained by simplifying the following equation and using eqns. (14)-(16):

$$\begin{aligned}\frac{\partial (JU)}{\partial t} + \frac{\partial F}{\partial \xi}J\frac{\partial \xi}{\partial x} + \frac{\partial G}{\partial \xi}J\frac{\partial \xi}{\partial y} + \frac{\partial H}{\partial \xi}J\frac{\partial \xi}{\partial z} + \frac{\partial F}{\partial \eta}J\frac{\partial \eta}{\partial x} + \frac{\partial G}{\partial \eta}J\frac{\partial \eta}{\partial y} + \frac{\partial H}{\partial \eta}J\frac{\partial \eta}{\partial z} \\ + \frac{\partial F}{\partial \zeta}J\frac{\partial \zeta}{\partial x} + \frac{\partial G}{\partial \zeta}J\frac{\partial \zeta}{\partial y} + \frac{\partial H}{\partial \zeta}J\frac{\partial \zeta}{\partial z} = 0.\end{aligned} \tag{17}$$

In this work, we proposed to solve eqn. (17) without any simplification, forcing the cancelation of the $I1$-$I3$ terms. A free stream preservation test, not given here, has confirmed the validity of this approach.

2.2 Numerical features.

The spatial derivatives are approximated with a 4th-order operator in addition to a stable high-order numerical boundary treatment based on the summation by parts (SBP) approach[11] . For time integration, a 3rd-order multi-stage Runge-Kutta explicit scheme is applied. A special feature of the code is that it applies the entropy splitting concept[21] to improve numerical stability, which is one of important issues for a DNS code that requires an extremely long run time to get the statistically converged results. The code parallelization has been achieved using the MPI library. Scalability and portability studies have been performed at various available HPC platforms.

The code used in this work is a modified version of the Shock/Boundary Layer Interaction (SBLI) code developed at the University of Southampton, adapted to the JISCF system. The SBLI code has been successfully used by previous researchers in the last years for different applications [16, 17, 18] .

3 The overlapping block-structured cylindrical grid.

3.1 Literature review.

A common issue in the simulation of fluid flows in circular geometries, which has limited the number of DNS studies in this field, is linked to the singularity present at the centerline ($r = 0$) when cylindrical-polar coordinates are used. This problem is not present when a finite volume formulation is applied[12] , or for a spectral-method-based solver[13]where a simple mesh can be adapted. With a finite difference approach the singularity at the centerline is evident and several solution have been proposed. For example, a staggered grid has been employed and the only quantity evaluated at $r = 0$ is the heat flux q_r which can be set to zero by definition or not involved in the calculation[22] . An alternative solution computing the velocity at the singular point as a combination of the Cartesian x and y components obtained from the radial and angular components on a staggered grid[14] . However, an intrinsic propriety of a structured grid in polar-cylindrical coordinates is that the number of points detected around the central axis is normally high with consequently very small time step.

Composite, or Chimera, grids consist of overlapping meshes and can be used to handle very complex geometries in a relatively easy way. However, the main drawback is the presence of an interpolation zone where two or more meshes overlap. Moreover, if more meshes are present and if high-order schemes are applied the computational effort to solve the interpolation area can be intensive and generate spurious oscillations which can be source of instability in turbulent flow.

Here we present a new approach based on overlapping meshes from different blocks without introducing any interpolation point or strong discontinuity in the derivatives of the spatial coordinates along the computational coordinates. The method has been successfully tested for a laminar flow in a pipe. The method is in the early stager of development and represents a starting point for further improvement and other possible applications, like round jet in cross flow or wing body junction flows.

3.2 Scheme and computational domain.

A possible solution for the circular geometry is sketched in Figure 2a: the grid is structured and can be decomposed into different blocks. However, the main drawback is the evident discontinuity of the spatial coordinate (x, y) along the computational (ξ, η) coordinates. These discontinuities can introduce spurious oscillations and then affect the stability and correctness of the simulation, especially for turbulent flow.

Figure 2b shows a Chimera grid obtained with two overlapping meshes. The main drawback is the need of an interpolation function in the overlapping region which can reduce the accuracy of the high order scheme and increase the computational costs.

The grid proposed here is based on five overlapping structured blocks (see Figure 3): 4 external blocks of a quarter of circle each and 1 internal block connected to the external blocks by overlapping. Since the number of points in each direction for each block has to be constant for a structured mesh, the internal block mesh will have some extra points overlapping on itself. These points are not used in the calculation of the flow field, but some special treatments need to be used at these points. Figure 4 shows a detail of the

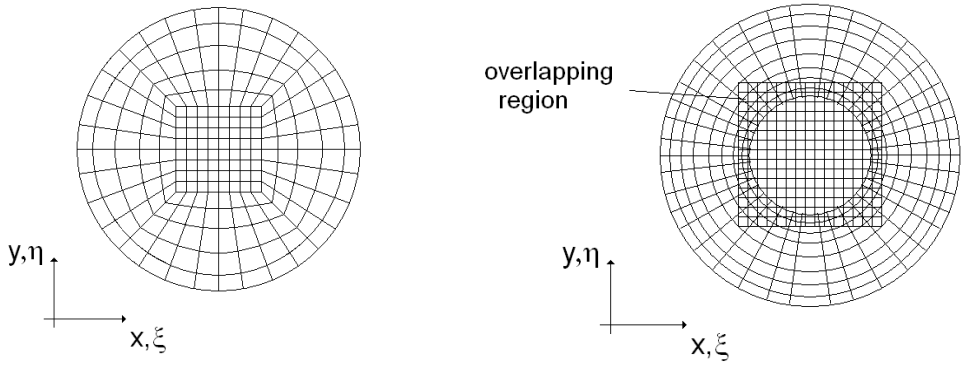

(a) A possible solution (b) Chimera grid

Figure 2: Meshes for circular geometries

ghost cells between the external blocks (4 and 1) and the internal one (5). The first derivative values along the row coordinate i, at the points (2,0), (1,0), (1,-1), (2,-1) and (2,-2), are evaluated as follows:

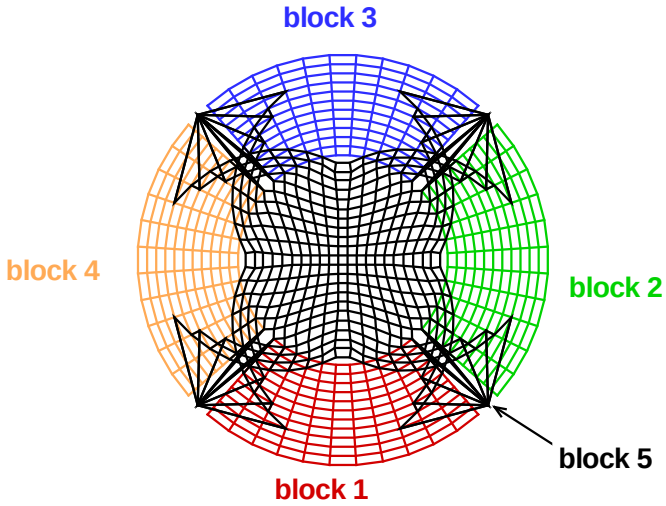

Figure 3: Sketch of 5 blocks configuration.

$$f'(2,0) = \frac{f(-1,1) + 8f(3,0) - 8f(1,0) - f(4,0)}{12\Delta h},$$
$$f'(1,0) = \frac{f(-3,2) + 8f(2,0) - 8f(-1,1) - f(3,0)}{12\Delta h},$$
$$f'(1,-1) = \frac{f(-4,2) + 8f(2,-1) - 8f(-2,1) - f(3,-1)}{12\Delta h},$$
$$f'(2,-1) = \frac{f(-2,1) + 8f(3,-1) - 8f(1,-1) - f(4,-1)}{12\Delta h},$$

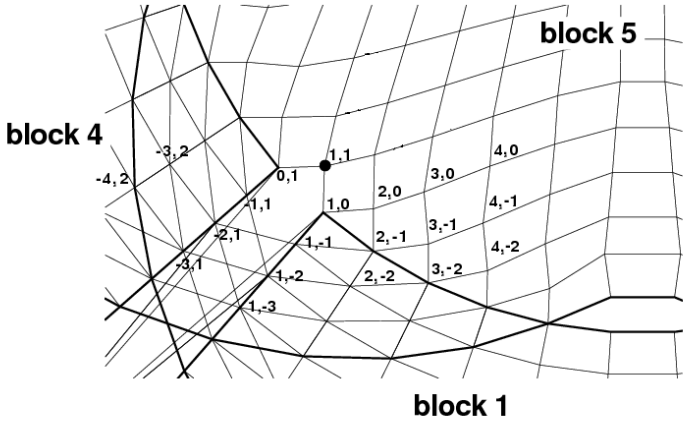

Figure 4: Derivatives in the 5-block configuration.

$$f'(2,-2) = \frac{f(-3,1) + 8f(3,-2) - 8f(1,-2) - f(4,-2)}{12\Delta h}.$$

A symmetric treatment is applied to the column coordinate j. The second derivative needs a special treatment only at the point (2,0):

$$f''(2,0) = \frac{-f(-1,1) + 16f(1,0) - 30f(2,0) + 16f(3,0) - f(4,0)}{12\Delta h^2}$$

When the metric derivatives are evaluated the above formulae are applied only for the first derivatives terms and only for the points (1,0) and (2,0). The group of terms given by $\frac{\partial}{\partial\xi}\left(J\frac{\partial\xi}{\partial x}\right)$, $\frac{\partial}{\partial\eta}\left(J\frac{\partial\eta}{\partial x}\right)$, etc. are evaluated with a second order central scheme and first derivatives in (1,-1,), (2,-1) and (2,-2) are not necessary.

3.3 Results: laminar flow in a pipe.

Firstly, a test case of laminar flow in a pipe has been carried out. The analytical solution is the well known Poiseuille solution: $v(r) = Re/4(-\partial p/\partial x)\delta^2\left[1-(r/\delta)^2\right]$. The grid is periodic in the streamwise direction and the flow is promoted by a constant pressure gradient $\partial p/\partial x = -1$. We choose as dimensional reference length $\delta = R$, where R is the radius of the pipe. The computational domain is $N_x \times N_y \times N_z$=11x11x2 for the external blocks and $N_x \times N_y \times N_z$=21x21x2 for the internal one. The solution, at $Re = 20$, $M_{cl} = 0.1$ and after 20 time units ($t\delta/u_{rif}$), is given in Figure 5. The difference between numerical solution and analytical value is $|w_{max} - w_{theory}| = \simeq 0.000522$.

The same test has been carried out with a finer grid of $N_x \times N_y \times N_z = 21 \times 21 \times 2$ for the external blocks and $N_x \times N_y \times N_z = 41 \times 41 \times 2$ for the internal one, and the results found present a slightly higher numerical error $|w_{max} - w_{theory}| = \simeq 0.000757$ (see Figure 6). This is inconsistent, considering that the error should be reduced by a fourth order power and it is probably due to the non continuity of the second spatial derivative as described in the next section.

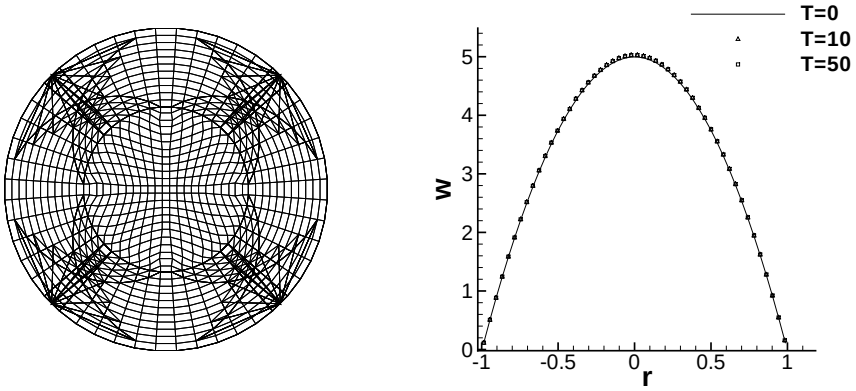

(a) (b)

Figure 5: Laminar flow in a pipe: coarse grid

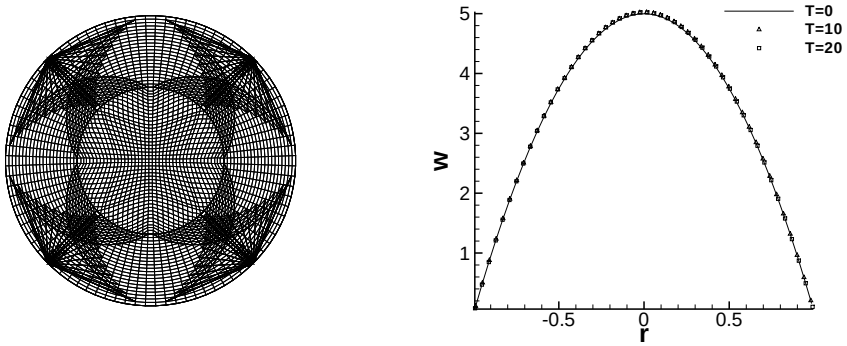

(a) (b)

Figure 6: Laminar flow in a pipe: fine grid

3.4 A better mesh.

The error previously found seems to be due to the discontinuity of the second derivatives at the center of the domain. In fact, the mesh is obtained from the intersection of polynomial functions and the continuity of the derivatives in each direction is not guaranteed. A better mesh can be built considering the union of two 3D-functions: a paraboloid function at the center of the cylinder and a spherical function at the extreme of the domain. Moving with the i, j indices along the radial direction r and the angular direction θ, the sum of the two functions is weighted by a tangent hyperbolic function normalized by the local maximum distance $(r - \sqrt{i^2 + j^2})$:

$$x = r\cos\theta f + i[1 + (i^2 + j^2)]g, \tag{18}$$

$$y = r\sin\theta f + j[1 + (i^2 + j^2)]g, \tag{19}$$

where

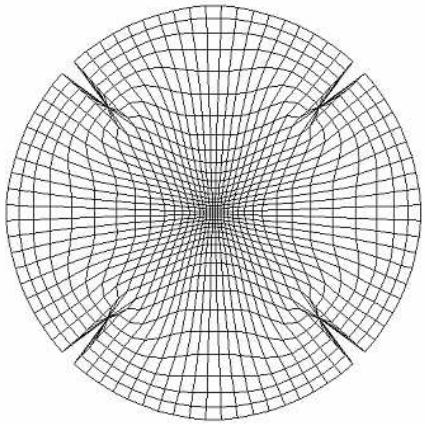

Figure 7: A better mesh for the cylindrical geometry.

$$f = \frac{\tanh\beta\sqrt{i^2+j^2}}{\tanh\beta}\frac{1}{r-\sqrt{i^2+j^2}}, \tag{20}$$

$$g = \frac{\tanh(1-\beta\sqrt{i^2+j^2})}{\tanh\beta}\frac{1}{r-\sqrt{i^2+j^2}}. \tag{21}$$

The result obtained is shown in Figure 7. The main advantages are not only the continuity of the second derivatives at the center of the domain, but, especially, the presence of no overlapping mesh as only 1 block is required. As in the previous case, special attention needs to be paid to the corner points where the mesh overlaps. Tests on this new configuration have not yet been completed.

4 Computational configuration for the JISCF case.

A sketch of the JISCF system is given in Figure 8a: the cross flow consists of two parallel walls and the round jet is injected from a nozzle exit located at the bottom wall. The nozzle is used to generate a sonic under-expanded jet. A total of 15 blocks are linked together in the following combination (see Figure 8b): blocks 1-5 for the nozzle geometry and jet inside the cross flow; blocks 6-13 for the junction between internal blocks and cross flow; block 14 for the inflow condition and block 15 for the outflow condition. With this arrangement it is possible to choose different lengths and shapes for the nozzle, inflow and outlet boundary without changing the block configuration. The number of points for each block is given in Table 1, with a total of 3,053,320 points.

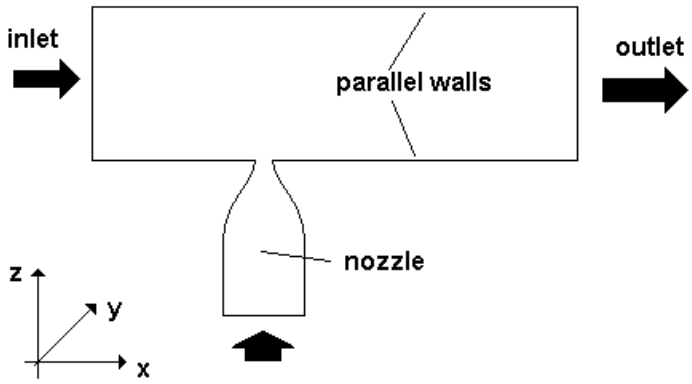

(a) Scheme.

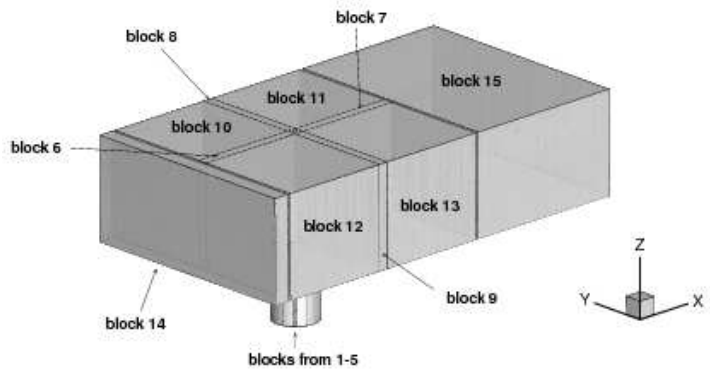

(b) Block configuration.

Figure 8: Scheme and block configuration of JISCF.

Figures 10a and 10b show cross sections of the JSICF mesh in the $x - z$ plane at $(y/D = 0)$ and in the $x - y$ plane at $(z/D = 0)$, respectively. Polynomial functions have been used for the stretching in all the three spatial directions. Choosing as reference length the half height of the channel $\delta = H/2$, the domain for the cross flow is $6.25\delta \times 2\delta \times 4.5\delta$ in

Block	N_x	N_y	N_z
1	12	12	202
2	12	12	202
3	12	12	202
4	12	12	202
5	22	22	202
6	62	12	140
7	62	12	140
8	12	62	140
9	12	62	140
10	59	59	140
11	59	59	140
12	59	59	140
13	59	59	140
14	6	130	140
15	22	130	140

Table 1: Number of points and resolution for JISCF coarse grid case

streamwise, normal and spanwise direction, respectively. The minimum and maximum grid resolutions, based on the Re_τ value later defined, are $\Delta x^+ = 0.89 - 13.25$, $\Delta z^+ = 0.9 - 9.35$ and $\Delta y^+ = 0.89 - 11.45$.

The flow conditions are similar to the experiments of Santiago and Dutton[3] , but at a much lower Reynolds number ($\simeq 1/27$ of experiment). Based on the wall inlet friction velocity $u_{\tau,in}$, bulk density at the inlet of the cross flow $\rho_{b,in}$, wall viscosity at inlet of the cross flow $\nu_{w,in}$ and the above reference length $\delta = H/2$, we have $Re_\tau = \rho_{b,in} u_{\tau,in} \delta / \nu_{w,in} = 180$. The corresponding value based on the centreline velocity is $Re_{cf} = \rho_{b,in} u_{cl,in} \delta / \nu_{w,in} \simeq 3400$. The Mach number, based on the same quantities, is $M_\tau = 0.065$ and $M_{cl} = 1.6$. The Reynolds number of the jet, based on the same previous bulk density, wall viscosity, jet diameter D and normal velocity at the exit of the jet $u_{jet,e}$ is $Re_{jet} = \rho_{b,in} u_{jet,e} D / \mu_{w,in} = 926$. In all the figures hereafter the spatial coordinates are non dimensionalized by the diameter D of the jet.

The no-slip condition is applied at the bottom and top walls of the cross flow, as well as on the nozzle walls. The velocity flow field at the inlet of the cross flow is obtained from a precursor turbulent channel simulation, while the density is obtained after extrapolation of the pressure field. This is necessary in order to avoid oscillations in the flow field. The same pressure extrapolation method is applied at the inlet of the nozzle, where the velocity is specified as a parabolic laminar profile (see next section). Non-reflecting boundary conditions are applied at the exit of the cross flow domain, while periodic boundary conditions are applied in the spanwise direction. This is equivalent to simulating an infinite series of parallel jets. However, we chosen a domain wide enough to avoid interactions coming from the periodic conditions, as we are interested in the flow dynamics of a single jet. The choice of a correct spanwise length has been verified a posteriori.

Two parameters are fundamental to determine the penetration height of the jet into the cross flow: the injection angle θ, defined as the angle between the axis of the jet and the wall

normal direction of the cross flow, and the flux momentum ratio $J = \rho_{jet,e} U_{jet,e}^2 / \rho_{b,in} U_{cf,in}^2$, where $\rho_{jet,e}$ is the mean density of the jet at the exit of the nozzle, $U_{jet,e}$ is the mean velocity of the jet in the wall normal direction of the cross flow, $\rho_{b,in}$ is the already defined bulk density at the inlet of the cross flow and $U_{cf,in}$ is the mean velocity of the cross flow at the inlet of the cross flow domain.

A total of 32 Cray XT4 nodes (128 cores) for about 55 hours have been used for each test case.

4.1 Inlet nozzle values.

To obtain an under-expanded sonic jet, an appropriate shape and flow conditions need to be applied to the nozzle domain. The nozzle used here (see Figure 9) has an inlet diameter $D_i = 4D$. The total length of the nozzle is equal to six jet diameter ($6D$), divided into one section with constant diameter ($L_c = 3.1D$) and another with variable diameter ($L_v = 2.9D$). The curvature is represented by a cubic function with zero derivative at the start and finish point of the curvature. The inlet conditions are obtained by imposing a parabolic laminar profile where the maximum velocity and temperature are obtained as follows (subscript cf, jet, in and jet, e indicate *crossflow*, *inlet of the jet nozzle* and *exit of the jet nozzle*, respectively):

1. Choose Re_τ, M_τ, the inlet diameter of the nozzle (and then the ratio between the areas $A_{jet,e}/A_{jet,in}$) and the flux momentum ratio $J = \rho_{jet,e} U_{jet,e}^2 / \rho_{b,in} U_{cf,in}^2 = \gamma P_{jet,e} M_{jet,e}^2 / (\gamma P_{cf,in} M_{cf,in}^2)$.

2. Choose the nozzle inlet maximum temperature ($T_{jet,in,max}$).

3. From the isentropic expansion relationships find the value of $\rho_{jet,in}/\rho_{jet,e}$, $p_{jet,in}/p_{jet,e}$, $T_{jet,in}/T_{jet,e}$ and $M_{jet,e}$ for the given ratio $A_{jet,e}/A_{jet,in}$.

4. From the statistics of the turbulent precursor channel simulation take the maximum cross flow velocity $U_{cf,in,max}$, the mean value $U_{cf,in}$, the max temperature $T_{cf,in,max}$, the mean temperature $T_{cf,in}$ and the mean pressure $P_{cf,in} = \rho_b T_{cf,in} / (\gamma M_{\tau,in}^2)$. Find the Mach value $M_{cf,in,max} = M_{\tau,in} U_{cf,in,max} / U_{\tau,in} \sqrt{T_w / T_{cf,in,max}}$.

5. Find $P_{jet,e} = J \gamma P_{cf,in} M_{cf,in}^2 / (\gamma M_{jet,e}^2)$

6. Find $T_{jet,in} = (T_{jet,in,max} - T_w) 4/5 + T_w$ (valid for a temperature profile in a laminar pipe flow), $P_{jet,in} = P_{jet,e} \times (sonic\ ratio)$, $\rho_{jet,in} = P_{jet,in} \gamma M_{\tau,in}^2 / T_{jet,in}$, $\rho_{jet,e} = \rho_{jet,in} / (sonic\ ratio)$, $V_{jet,e} = \sqrt{\rho_{cf,in}/\rho_{jet,e} J}\ U_{cf,in}$, $V_{jet,in} = \rho_{jet,e} V_{jet,e} A_{jet,e} / (\rho_{jet,in} A_{jet,in})$ (continuity equation) and $V_{jet,in,max} = 2 V_{jet,in}$.

7. Finally, verify that the nozzle inlet Mach value $M_{jet,in} = M_{\tau,in} V_{jet,in} / u_{\tau,in} \sqrt{T_w / T_{jet,in}}$ matches with the sonic value found at step 3.

4.2 Configuration without nozzle.

The first test case on the JISCF has been carried out for $\theta = 90°$ and $J = 1$. Because the exit of the jet is supposed to be sonic, a comparison with a similar configuration,

but without resolving the nozzle domain, has been carried out. The inlet of the jet has been simulated with a fixed profile on the bottom wall of the cross flow. The domain chosen is $6\delta \times 2\delta \times 4.5\delta$ in streamwise, normal and spanwise direction, respectively, while the minimum and maximum grid resolution, based on the Re_τ value defined later, are $\Delta x^+ = 2.16 - 10.74$, $\Delta z^+ = 0.74 - 3.96$ and $\Delta y^+ = 0.95 - 8.82$. The mesh is stretched with a cubic function in the streamwise direction, a tangent hyperbolic function in the normal direction and a fifth order polynomial function in the spanwise direction in order to guarantee the continuity of the spatial derivatives up to fourth order. The same boundary conditions of the JISCF are applied and the jet inlet profile is defined as: $\rho_{jet,in} = 1$, $\rho u_{jet,in} = J u_{cf,in}$, $\rho v_{jet,in} = \rho w_{jet,in} = 0$ and $T_{jet,in} = 1$. The computational effort for this configuration is smaller than the JISCF, as 16 Cray XT4 nodes (64 cores) are used and about 72 hours are required for each test case.

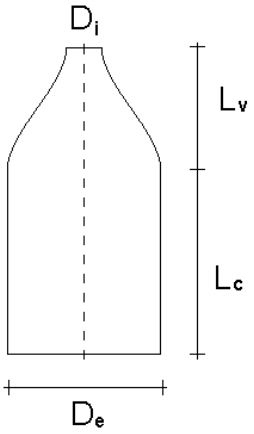

Figure 9: Scheme of the nozzle domain.

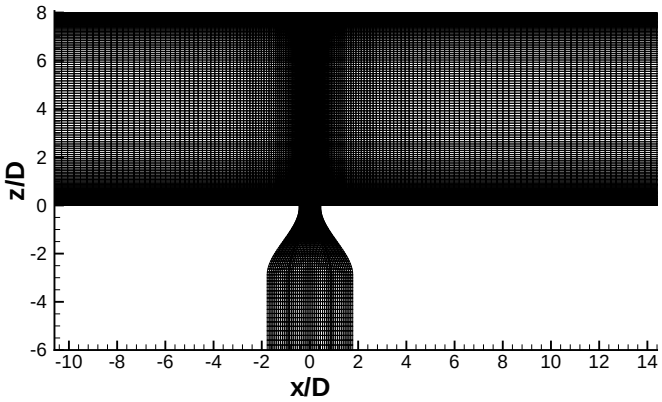

(a) $x - z$ plane at $y/D = 0$.

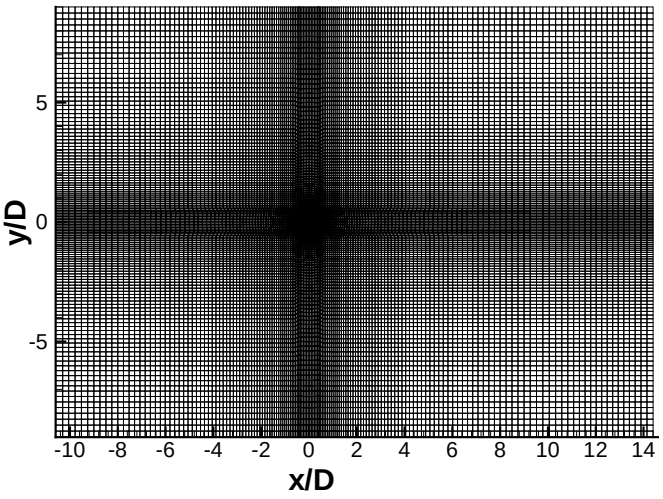

(b) $x - y$ plane at $z/D = 0$.

Figure 10: Cross section of JISCF mesh.

5 Precursor turbulent channel.

A precursor turbulent plane channel has been run in order to generate the inflow data for the JISCF. The idea is to generate a sequence of instantaneous slices in the $y-z$ plane and then, by spatial and time interpolation, to feed into the JISCF domain the turbulent flow field (see Figure 11). Choosing as reference length the half height of the channel ($\delta = H/2$), the domain is $6\delta \times 2\delta \times 4.5\delta$ in the normalized streamwise (x), wall-normal (z) and spanwise (y) direction, respectively. The number of points is $88 \times 125 \times 95$ and the resolution is $\Delta x^+ = 12.41$, $\Delta z^+ = 0.77-7.20$ and $\Delta y^+ = 6.5$. Ten points are present in the viscous sub-layer region ($y^+ \leq 10$). Based on the friction velocity, bulk density and wall conditions, we chose $Re_\tau = \rho_b u_\tau H/\mu_w = 180$ and $M_\tau = u_\tau/\sqrt{\gamma R T_w} = 0.07$. The corresponding centreline values are $Re_{cl} = \rho_b u_{cl} H/\mu_{cl} \simeq 3400$ and $M_{cl} = u_{cl}/\sqrt{\gamma R T_{cl}} = 1.6$. Periodic boundary conditions are applied in the streamwise and spanwise directions and the flow is forced by a constant pressure gradient $\partial P/\partial x = -1$. As initial condition has been used a mean profile, obtained following the law of the wall and the log wall, plus correlated perturbations[17] . An uniform mesh is applied in the streamwise and spanwise directions while a hyperbolic tangent stretching is applied in the wall-normal direction. Instantaneous slices of the turbulent channel are saved every 5 iteration ($\simeq 0.0013\Delta t$). Each simulation required the use of 8 Cray XT4 (nodes) (32 cores) for approximately 18 hours.

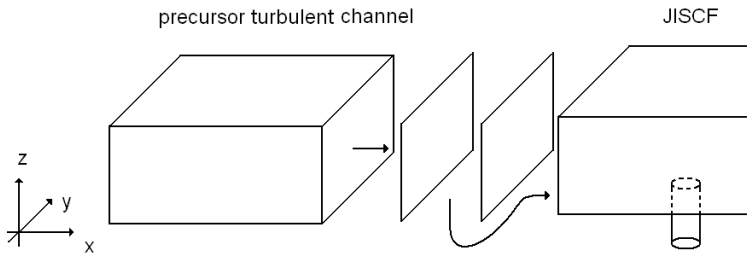

Figure 11: Sketch precursor turbulent channel - JISCF system.

In the practical applications, the core of the fluid is typically colder than the wall temperature [18] . To reproduce a similar situation, a heat sink term ($\dot{Q} = h(T - T_{cl,0})$ has been added in the energy equation. To validate this idea, we ran a test case at $M_{cl} = 3$ and $T_w = 3$. The target temperature is the isentropic value at the centreline Mach number: $T_{cl,0} = T_w/(1 + (\gamma - 1)/2M_{cl}^2)$=1.07. The heat transfer coefficient h has been chosen equal to 100 and the data are compared with a boundary layer profile at same Mach number[19] on Figure 12. The comparison has been made considering that the boundary layer thickness found in the plane channel is $\delta_{0.99} = \delta_0 = 0.8$ and, at $M_\infty = 3$ the ratio between displacement boundary layer thickness and boundary layer thickness is $\delta_1/\delta_0 = 0.324/0.865$ [19] . The profile is similar in the viscous sub-layer region and close to the centre of the channel, but different in between of these two regions. The profile for the mean streamwise momentum ρu and the mean streamwise velocity u present differences as well. Ideally, we should use a sink of energy which is a function of the normal wall distance in order to obtain a more realistic profile.

For the $M_{cl} = 1.6$ case, we have chosen $h = 1000$ and found the profile given in Figure 13. After a transient period of 10 time units ($u_\tau t/H$), statistical data have been

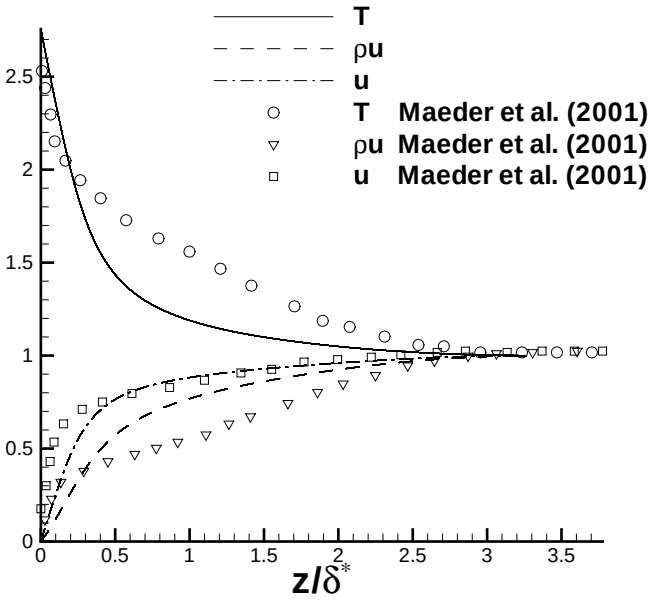

Figure 12: Comparison between present results and Maeder et al. (2001) data at $M_\infty = 3$

collected for the successively 10 time units and averaged in the streamwise and spanwise direction. Turbulent intensity values and Reynolds shear stress are given in Figures 14 and 15, respectively, and compared with previous DNS data at $M_\tau = 0.1$[21] . Results agree fairly well and small difference are probably due to the different Mach numbers used.

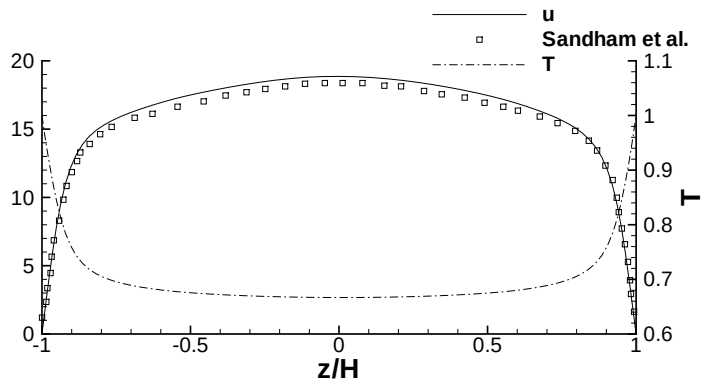

Figure 13: Precursor turbulent channel: mean streamwise velocity.

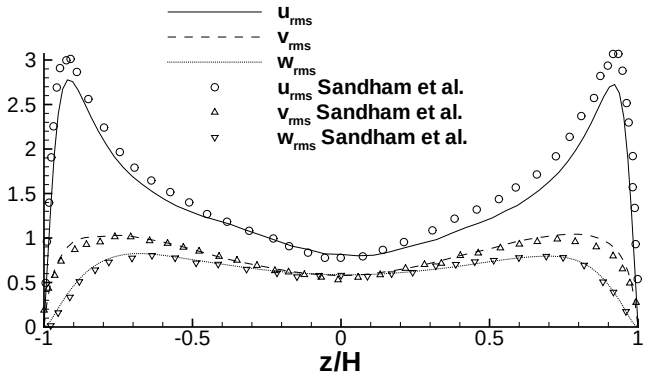

Figure 14: Precursor turbulent channel: turbulent intensity.

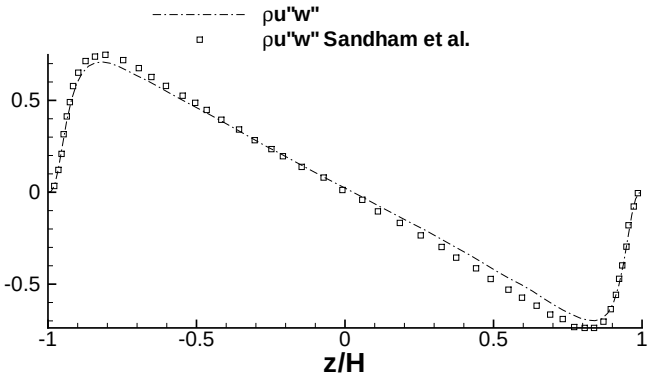

Figure 15: Precursor turbulent channel: shear stress.

6 Results at $\theta = 90°$ and $J = 1$: comparison with no-nozzle configuration.

In the following we present numerical results for the JISCF obtained with an injection angle $\theta = 90°$ and momentum ratio $J = 1$ (hereafter indicated as test A). A comparison with the no-nozzle configuration (hereafter case B) is presented in order to show the effect of the nozzle on the jet penetration into the cross flow.

The data have been collected after a transient time of 2 time units (around 3 through-flow times) and then for 8 time units (around 12 through-flow times) until statistical convergence is achieved and verified. Results are divided in three parts: mean values, turbulence intensities and instantaneous field.

6.1 Mean values.

Figures 16a and 16c show the mean concentration of the passive scalar C at the middle plane ($y = 0$) for test cases A and B, respectively. The profiles are quite similar, but some differences can be observed in the concentration downstream of the jet and in the close-up view Figures (16b and 16d): in case A the passive scalar seems to be transported more in the streamwise direction than in case B. Moreover, in case B the scalar seems to have upstream a stronger diffusion than case A at the inlet of the jet. The penetration height h, defined as the wall normal distance where the concentration of the passive scalar is 0.01%, is similar at the jet exit but slightly higher in case B moving downstream. The close-up view on Figure 16f (the straight red lines indicate the jet exit location) confirms the upstream diffusion present in case B. A different situation is present in the $x - y$ plane (see Figure 17a-c obtained at $z/D = 0.5$): in case A the passive scalar is transported further in the spanwise direction than in case B. The red circle in 17c represents the jet exit location. Finally, from Figure 18a to 18o it is possible to observe the propagation of the passive scalar in the $y - z$ plane at different streamwise locations: at $x/D = 0$ we have $h = 1.4$ for both cases. Moving downstream, the penetration height achieves the value of 2.0 for case A and 2.2 for case B at $x/D = 2$. The diffusion present in case B is here smaller, probably due to the smaller gradient of the passive scalar in the spanwise direction.

Figures 19a and 19b shown density contours and streamlines in the centre plane $y/D = 0$ respectively for case A and case B. In both case the compression is quite strong, nearly as a shock wave (however, an analysis of the magnitude of the gradient of the density $|\nabla\rho|$ does not confirm the presence of a strong shock wave). The jet is merging into the streamwise flow in a distance less than two diameters in the wall normal direction. Upstream of the jet exit, it is possible to observe the recirculation zone associated with a separation of the incoming boundary layer (see Figures 20a and 20b. As usual, the straight red lines indicates the jet exit location.). The centre of the recirculation is at $x/D = -0.44$ and $z/D = 0.1$ for case A and at $x/D = -0.49$ and $z/D = 0.034$ for case B. The centre of the separation is at $x/D = -0.71$ and $z/D = 0.15$ for case A and at $x/D = -0.78$ and $z/D = 0.17$ for case B. The separation point is at $x/D = -1.51$ and $x/D - 1.88$, respectively for case A and B.

Figures 21a and 21b show the density contours and streamlines in the $x - y$ plane at $z/D = 0.5$. A counter rotating vortex pair (CRVP) is observed just downstream the jet

exit. This CRVP increases in strength moving downstream as also visualized in Figure 22a-b and Figure 23a-b obtained at $x/D = 0$ and $x/D = 1$, respectively. From the same Figures, comparing case A and B it noted that the density field is quite similar between the two cases.

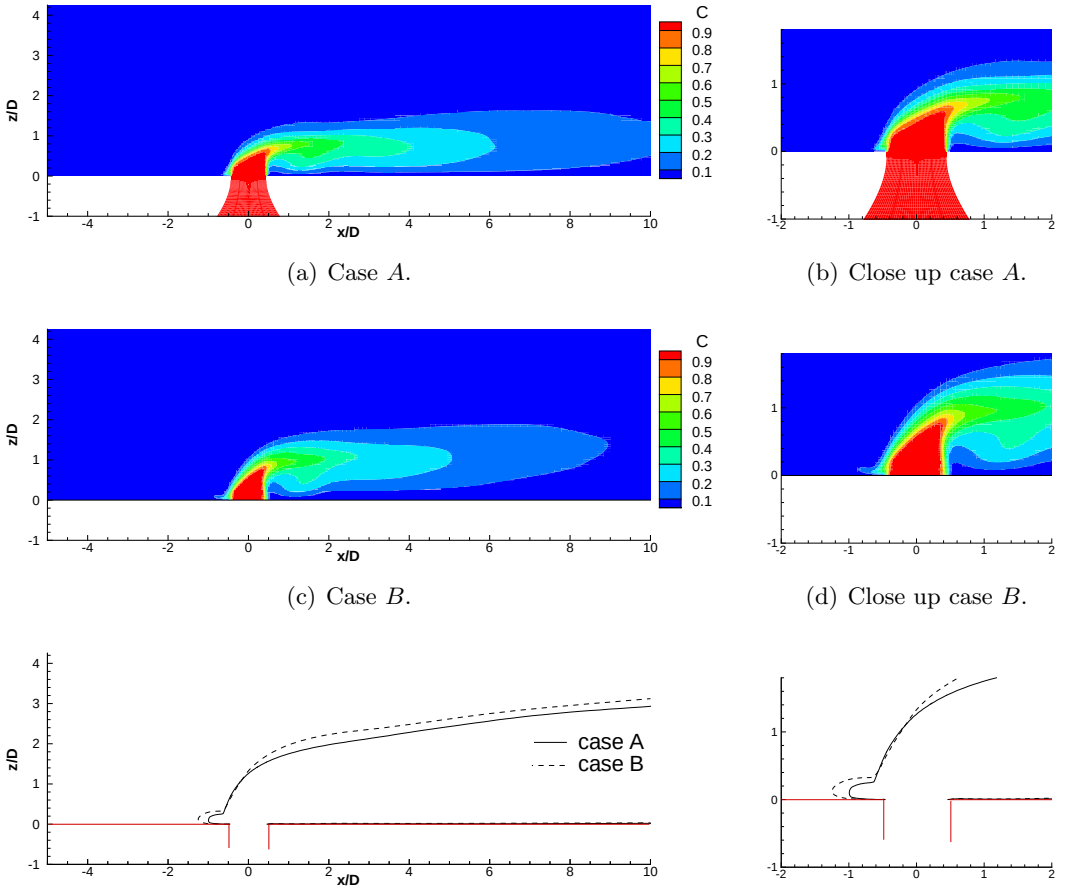

(a) Case A.

(b) Close up case A.

(c) Case B.

(d) Close up case B.

(e) $C = 0.01\%$ contour.

(f) Close up of the comparison.

Figure 16: Scalar field in the middle plane ($y/D = 0$).

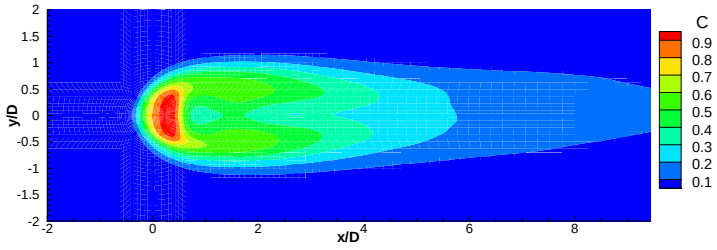

(a) Case A.

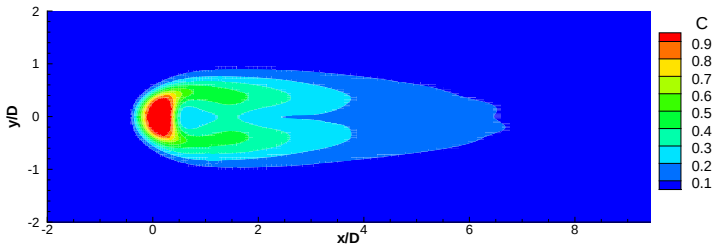

(b) Case B.

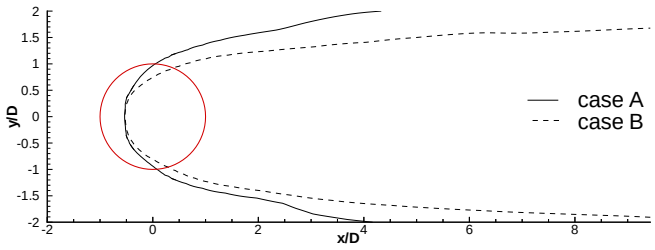

(c) $C = 0.01\%$ contour.

Figure 17: Scalar field in the $x - y$ plane at $z/D = 0.5$.

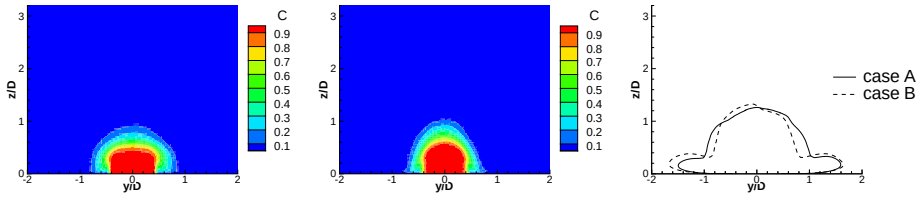

(a) Case A at $x = 0$. (b) Case B at $x = 0$. (c) Comparison at $x = 0$.

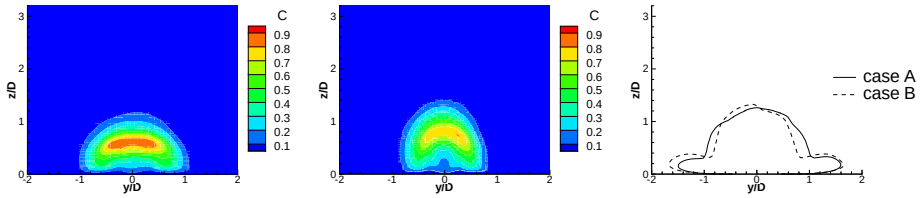

(d) Case A at $x = 0.5$. (e) Case B at $x = 0.5$. (f) Comparison at $x = 0.5$.

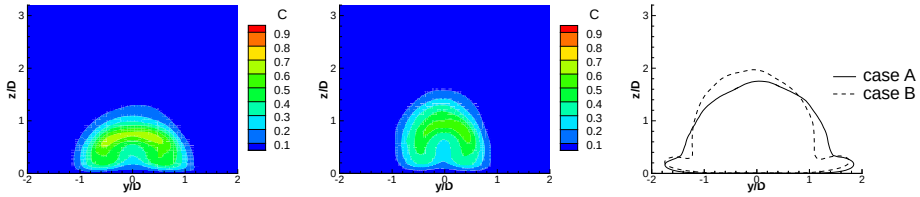

(g) Case A at $x = 1$. (h) Case B at $x = 1$. (i) Comparison at $x = 1$.

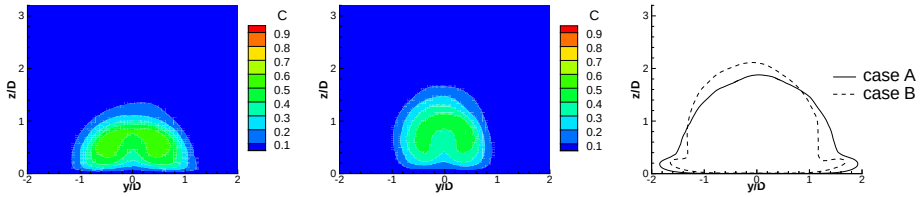

(j) Case A at $x = 1.5$. (k) Case B at $x = 1.5$. (l) Comparison at $x = 1.5$.

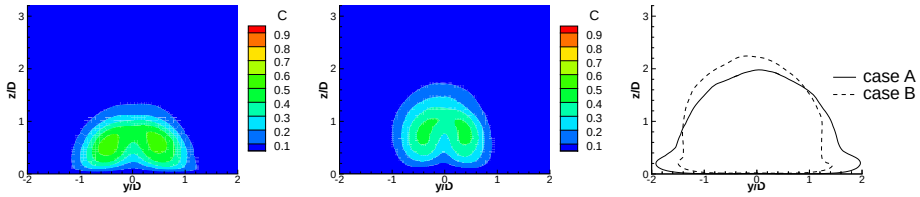

(m) Case A at $x = 2$. (n) Case B at $x = 2$. (o) Comparison at $x = 2$.

Figure 18: Scalar field in the $y - z$ plane at different streamwise locations.

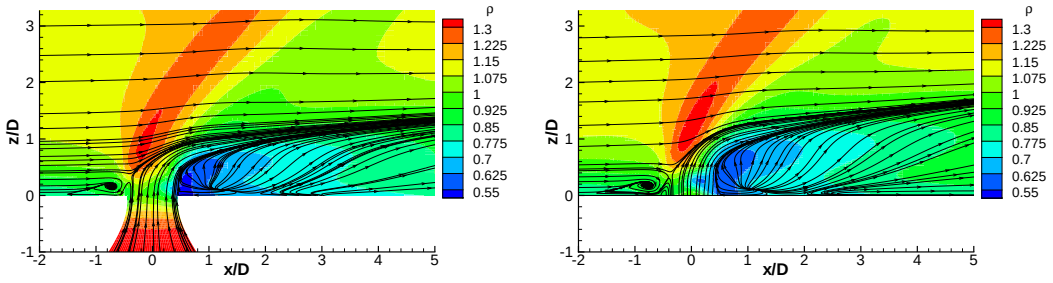

(a) Case A. (b) Case B.

Figure 19: Density contour plot and streamline in the centre plane ($y = 0$).

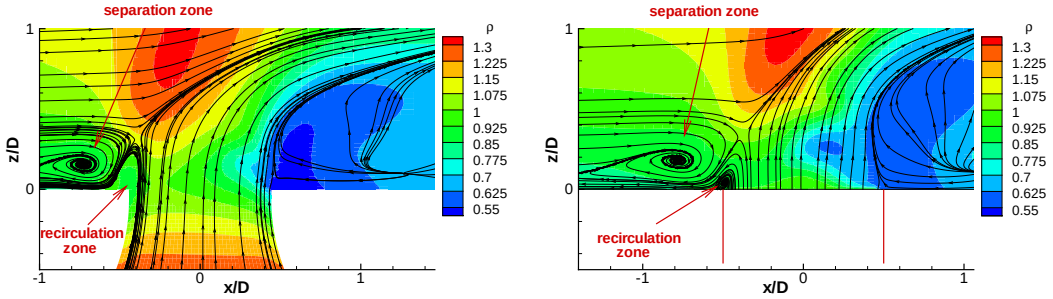

(a) Case A. (b) Case B.

Figure 20: Density contour plot and streamline in the centre plane ($y = 0$).

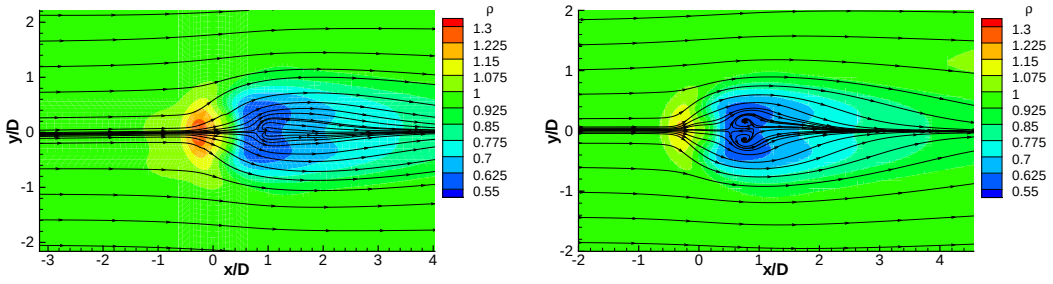

(a) Case A. (b) Case B.

Figure 21: Density contour plot and streamline in the $x - y$ plane at $z = 0.5$.

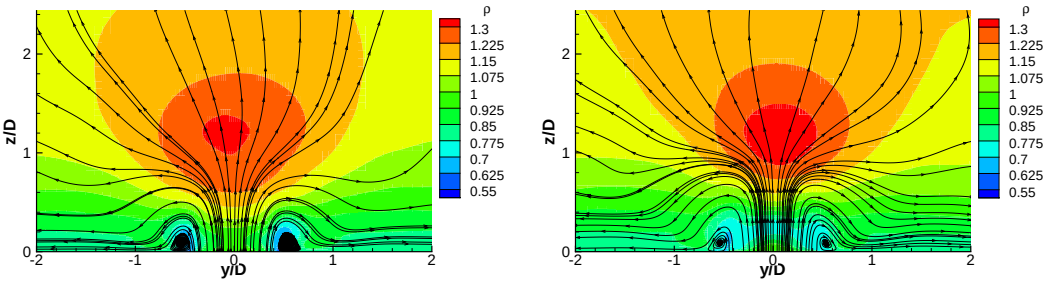

(a) Case A. (b) Case B.

Figure 22: Density contour plot and streamline in the $y-z$ plane at $x=0$.

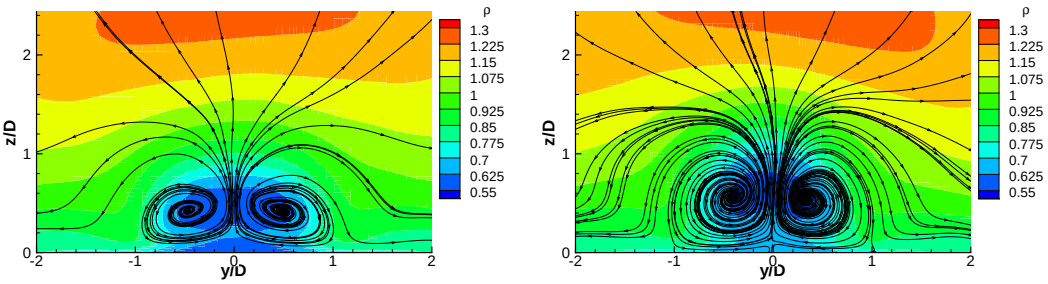

(a) Case A. (b) Case B.

Figure 23: Density contour plot and streamline in the $y-z$ plane at $x=1$.

6.2 Turbulent intensities.

Turbulent intensity values for both case A and B are presented in Figure 24a-c. The values are normalized by the maximum streamwise velocity u_{max}, which is 19.3 and 19.4 respectively for case A and B. Three different streamwise location have been chosen: $x/D = -8$ (inlet of the cross flow), $x/D = 0$ (jet axis) and $x/D = 16$ (outlet of the cross flow). The values referee to the middle plane location $y/D = 0$ and are not averaged in the spanwise direction. At the inlet of the cross (Figure 24a) flow good agreement between the two test cases has been found. Only the u_{rms} quantities are slightly different close to the walls. Similar agreement is found for the u_{rms}, v_{rms} and the $u\prime w\prime$ quantities on the jet axis (24b), while the w_{rms} seems to have a similar behavior with a peak close to the lower wall ($z/D = 0$) strongly increased by the presence of the jet. In fact, while at the inlet of the domain $w_{rms} = 0.04$ for both cases, in presence of the jet we have 0.21 and 0.25 respectively for case A and case B. Moreover, the location of the peak in the wall normal distance is slightly higher for the test case A. Finally, at the exit of the domain (Figure 24c) same consistency observed at the inlet is found. Moreover, the flow seems to have not lost most of the inlet turbulence.

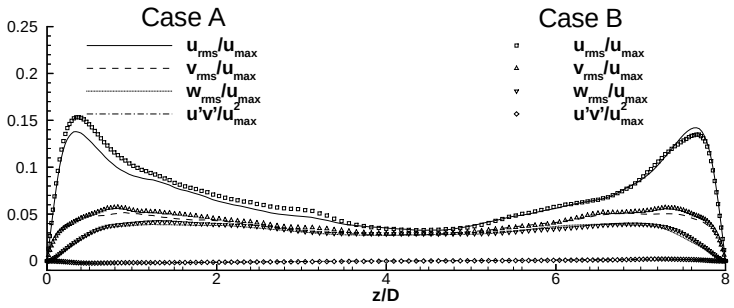

(a) $x = -8$.

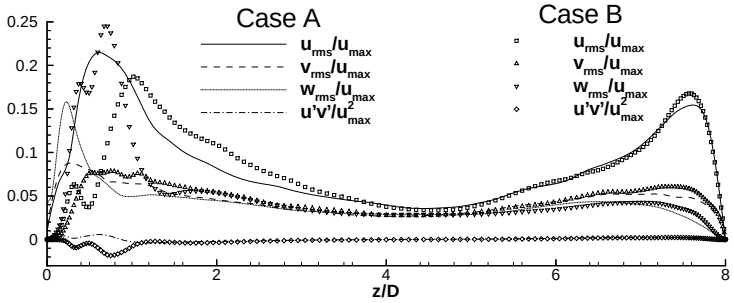

(b) $x = 0$.

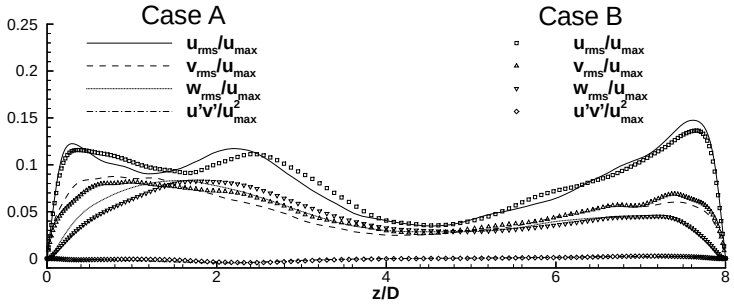

(c) $x = 16$.

Figure 24: Turbulent intensities values at different streamwise locations.

6.3 Instantaneous values.

The instantaneous flow field here presented is obtained after a total of 10 time units (about 15 trough flow). In Figure 25a and 25b are shown the streamwise velocity u at the middle plane ($y/D = 0$). The maximum speed found is 19.1 for case A and 21.6 for case B.

Considering that we are injecting a hot jet in a cold cross flow, it is interesting to observe the mixing heat along the streamwise direction. In Figure 25a and 25b are shown the temperature contour plot at the middle plane $y/D = 0$ for case A and B, respectively. Since we used a Prandtl number nearly equal to the Schimdt number (0.72 and 1, respectively), we expect a similar behavior between the temperature and the passive scalar variables. Figure 25e and 25f show the passive scalar for test case A and B, respectively. However, same main difference can be observed due to the different boundary conditions applied. In fact, while the passive scalar is unitary only inside the nozzle domain, the temperature has unitary value also on the walls of the cross flow domain. A thermal boundary layer is then present on top and bottom walls and the bulk region receives a heat transfer from both walls plus the incoming jet.

Finally, Figure 25g and 25h show the isosurface of the streamwise vorticity for case A and B, respectively. Due to the low Reynolds number used the structures seem to be quite thick and mainly representative of the jet injection flow field (i.e. no small structures due to an increment of the turbulence seem to be present). The isosurface are colored by the pressure value.

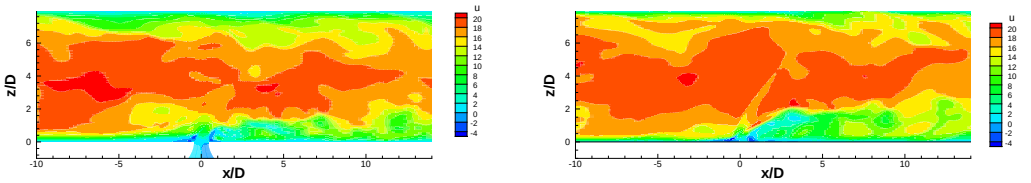

(a) Case A.

(b) Case B.

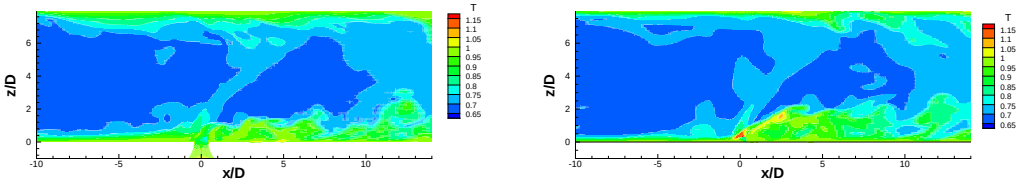

(c) Case A.

(d) Case B.

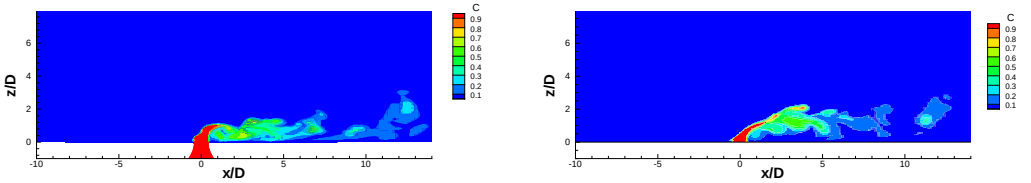

(e) Case A.

(f) Case B.

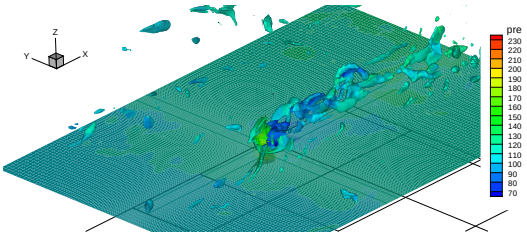

(g) Case A.

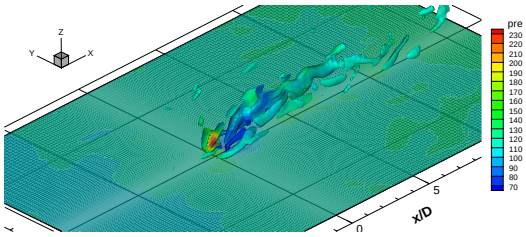

(h) Case B.

Figure 25: Instantaneous results.

7 Summary.

Direct numerical simulations of a round jet in supersonic cross flow have been carried out. The flow inside the cylindrical domain has been solved by use of an overlapping mutliblock structured grid. This method has been validated with simulations of laminar flow in a pipe, but grid convergence tests show an anomalous behavior probably due to a discontinuity in the second derivatives at the center of the cylindrical mesh. A better mesh has been proposed, but not tested. A new formulation of the fully 3D curvilinear form of the Navier-Stokes equations is proposed; the advantage is the avoiding of complicate average for high order schemes. The inlet profile of the JISCF system is generated by a precursor turbulent boundary layer simulation, where a sink of energy has been used in order to reproduce flow dynamic conditions more similar to SCRAMJET applications. A comparison with boundary layer results at same Mach number shows the validity of the approach, but a better function for the sink of energy should be used. A passive scalar variable has been used in order to investigate the penetration high of the jet into the cross flow. However, due to a lack of resolution, a forcing filter has been used in order to maintain the value between zero and the unity. The results for the JISCF case at $\theta = 90^\circ$ and $J = 1$ have been compared with a configuration without nozzle, where the jet is applied with a fixed profile on the bottom wall of the cross flow. Results show good agreement, but some difference can be observed: the JISCF seems to have a slightly higher penetration when the nozzle geometry is not considered. The flow topology analysis is in agree with previous experimental and numerical work, a part the absence of 3D shocks probably due the low Reynolds number used. Successively tests at different injection angle and flux moment ratio are planned as future work.

References

[1] Ben-Yakar, A. and Mungal, M.G. and Hanson, R.K. (2006). Time evolution and mixing characteristics of hydrogen and ethylene transverse jets in supersonic crossflows *Physics of Fluids*, **18**, 026101.

[2] Gruber, M.R. and Nejad, A.S. and Chen, T.H. and Dutton, J.C. (1997). Compressibility effects in supersonic transverse injection flowfields, *Physics of Fluids*, **9**, 1448-1461.

[3] Santiago, J.G. and Dutton, J.C., (1997). Velocity measurements of a jet injected into a supersonic crossflow, *Journal of Propulsion and Power*, **13**,(2).

[4] Everett, D.E. and Woodmansee, M.A. and Dutton, J.C. and Morris, M.J. (1998). Wall pressure measurements for a sonic jet injected transversely into a supersonic crossflow, *Journal of Propulsion and Power*, **14**, 6, 861-868.

[5] VanLerberghe, W.M. and Santiago, J.G. and Dutton, J.C. and Lucht, R.P. (2000). *AIAA journal*, **38**, 3, 470-479

[6] Kawai, S. and Lele, S.K., (2008). Mechanisms of jet mixing in a supersonic crossflow: a study using large-eddy simulation, *AIAA Paper*, **4575**.

[7] Lin, K-C., Ryan, M., Campbell C., (2008). Scalability of Ethylene Gaseous Jets for Fueling Scramjet Combustor at Various Scales, *Unpublished*.

[8] Chenault, C.F. and Beran, P.S. and Bowersox, R.D.W. (1999). Numerical investigation of supersonic injection using a Reynolds-stress turbulence model, *AIAA journal*, **37**, 10, 1257–1269.

[9] Lavante, E. and Zeitz, D. and Kallenberg, M. (2001). Numerical Simulation of Supersonic Airflow with Transverse Hydrogen Injection, *Journal of Propulsion and Power*, **17**, 6, 1319–1326.

[10] Peterson, D. M., Subbareddy, P. K. and Candler, G. V. (2006). Assessment of synthetic inflow generation for simulating injection into a supersonic crossflow, *AIAA Paper*, 8128.

[11] Carpenter, M.H. and Nordstrom, J. and Gottlieb, D. (1999). A stable and conservative interface treatment of arbitrary spatial accuracy, *Journal of Computational Physics*, **148**, 2, 341–365.

[12] Eggels, J.G.M., Unger, F., Weiss, M.H., Westerweel, J., Adrian, R.J., Friedrich, R. and Nieuwstadt, F.T.M. (1994) Fully developed turbulent pipe flow: a comparison between direct numerical simulation and experiment, *J. Fluid Mech*, **268**, 175–209.

[13] Shan, H., Ma, B., Zhang, Z. and Nieuwstadt, F.T.M. (1999) Direct numerical simulation of a puff and a slug in transitional cylindrical pipe flow, *Journal of Fluid Mechanics*, **387**, 39–60.

[14] Fukagata, K. and Kasagi, N. (2002). Highly energy-conservative finite difference method for the cylindrical coordinate system, *Journal of Computational Physics*, **181**, 2, 478–498.

[15] Ferziger, J.H., Peric, M., Morton, K.W. (1999) Computational methods for fluid dynamics,

[16] Lawal, A.A. and Sandham, N.D. (2001). Direct simulation of transonic flow over a bump, *Direct and Large-Eddy Simulation IV*, 301–310.

[17] Li, Q. (2003). Numerical study of mach number effects in compressible wall-bounded turbulence, *PdH thesis at Southampton University*

[18] Krishnan, L. and Sandham, N.D. (2006). On the merging of turbulent spots in a supersonic boundary-layer flow, *International Journal of Heat and Fluid Flow*, **27**, 4, 542–550.

[19] Maeder, T. and Adams, N.A. and Kleiser, L. (2001). Direct simulation of turbulent supersonic boundary layers by an extended temporal approach, *Journal of Fluid Mechanics*, **429**, 187–216

[20] Thomas, P. D. and Lombard, C. K., (1979). Geometric conservation law and its application to flow computations on moving grids, *AIAA Journal*, taxtbf 17, 10, 1030.

[21] Sandham, N.D., Li Q. and Yee, H.C., (2002) Entropy splitting for high order numerical simulation of compressible turbulence, *Journal of Computational Physics*, **178**,307-322

[22] Verzicco, R. and Orlandi, P., (1996) A finite-difference scheme for three-dimensional incompressible flows in cylindrical coordinates, *Journal of Computational Physics*, **123**,402-414

[23] , Pulliam, T.H. and Steger, J.L. (1980) Implicit finite-difference simulations of three-dimensional compressible flow *AIAA Journal*, **18**,159-167